Characterization of oxidative processes associated to low-severity tire tread wear

Cloé Chanal, Jules Galipaud, Benoît Moreaux, Jean-Luc Loubet, P Sotta

Wear 566–567 (2025) 205753

Contents lists available at ScienceDirect

Wear

journal homepage: www.elsevier.com/locate/wear

Characterization of oxidative processes associated to low-severity tire tread wear

C. Chanal [a,b,*], J. Galipaud [b,c], B. Moreaux [d], J.-L. Loubet [b], P. Sotta [a,**]

[a] INSA Lyon, Université Claude Bernard Lyon 1, Université Jean Monnet, CNRS UMR 5223, Ingénierie des Matériaux Polymères, 17 Av. Jean Capelle, Villeurbanne Cedex, F-69621, France
[b] Ecole Centrale de Lyon, CNRS UMR 5513, Laboratoire de Tribologie et Dynamique des Systèmes, 36 avenue Guy de Collongue, F-69134, Ecully, France
[c] INSA Lyon, Université Claude Bernard Lyon 1, CNRS UMR 5510, MATEIS, Villeurbanne Cedex, F-69621, France
[d] Solvay Silica, 15 rue Pierre Pays, Collonges-au-Mont-D'Or, F-69660, France

ARTICLE INFO

Keywords:
Wear
Tribometer
Rubber
Oxidation

ABSTRACT

As the tire tread wears throughout its lifetime, particles are generated due to small-scale fracture processes. Friction and wear may also involve physico-chemical degradation of the material. In this paper, the chemical effects associated to low-severity wear of filled Styrene Butadiene Rubber (SBR)/cis-Butadiene Rubber (BR) materials were investigated. Laboratory wear tests were performed using a home-made rotary tribometer in which intermittent sliding contacts on a slightly rough granite surface are applied. This enables imitating real conditions in terms of kinematics and dynamics of the contact for tire treads. The resulting wear patterns were analyzed through X-ray Photoelectron Spectroscopy (XPS) and Scanning Electron Microscopy (SEM). The results show that sulfur oxidation occurs concomitantly to wear. Besides, thermal measurements reveal no significant temperature increase at the sample surface during the wear tests. This suggests that the observed chemical changes are not thermally activated but are instead due to mechanical phenomena related to interface shear. Analysis of the wear debris indicates that their chemical composition is consistent with that of the wear patterns.

1. Introduction

The wear particles generated by tires sliding on the road surface are a significant source of microplastics released into the environment [1,2]. According to Wagner et al. (2018) about 1.3 million tons of tire wear debris are generated in Europe per year [3]. Minimizing tire wear and/or controlling nature and size distribution of tire wear particles is thus a major challenge. On the other hand, other usage properties such as adherence and rolling resistance must be concomitantly optimized, which strongly constraints the specifications and formulation of appropriate rubber materials.

Evaluating wear properties of representative rubber materials is a challenging task. In-field tests are extremely costly, and tire wear is difficult to predict. Many parameters can have a large impact on the wear rate like tire, road and vehicle characteristics but also climate conditions and driving habits.

The most representative usage conditions correspond to low to very low severity wear, as a personal car tire should last over typically 100 000 km. This performance corresponds to a wear rate (in terms of height loss in the tread) of a few tens of nanometers per driven kilometer. Low and very low severity wear is difficult to assess in a controlled, reproducible way [4]. A dynamic tribometer was specifically designed to meet this challenge. This device was described in Ref. [5]. It reproduces dynamic, intermittent contacts with levels of pressure comparable to those in real conditions. Dynamic specifications in terms of contact time and sliding velocity are also close, even though not identical to real conditions. At the same time, it enables accumulating a large sliding length within a short period of time, thus providing the opportunity to perform *accelerated* wear tests, which is a key achievement.

First, it is essential to note that wear is associated to sliding motion which can be global or local [6]. Global, macroscopic sliding of the tire on the road surface occurs for example during braking or skidding, while local sliding phenomena are explained by physical phenomena. Indeed, even when a vehicle is travelling in straight line at a constant velocity,

* Corresponding author. INSA Lyon, Université Claude Bernard Lyon 1, Université Jean Monnet, CNRS UMR 5223, Ingénierie des Matériaux Polymères, 17 Av. Jean Capelle, Villeurbanne Cedex, F-69621, France.
** Corresponding author.
E-mail addresses: cloe.chanal@insa-lyon.fr (C. Chanal), paul.sotta@insa-lyon.fr (P. Sotta).

https://doi.org/10.1016/j.wear.2025.205753
Received 25 October 2024; Received in revised form 11 January 2025; Accepted 18 January 2025
Available online 24 January 2025

with no applied drive torque, sliding occurs at the trailing edge of the contact zone due to compression of the tread [4,6]. In the contact zone, the tread material is laterally compressed due to the difference between the arc and chord lengths (see Fig. 1). This lateral compression generates a tangential stress which eventually becomes larger than the local friction coefficient μ times the normal stress, thus generating sliding at the rear of the contact zone.

Typical orders of magnitude are as follows. The average normal pressure (tire pressure) corresponds to the supported weight per tire divided by the contact area. A normal pressure of the order $P = 0.3\times 10^6$ Pa (for a passenger car) and a normal force of the order 2.5×10^3 N are applied on each tire. It results in a width of the contact area $2a \approx 4\times 10^{-2}$ m and a deformed height $\delta \approx a^2/2R \approx 0.7$ mm (see Fig. 1), for a typical tire geometry with a radius $R = 0.3$ m and a width of 0.2 m. The difference between the arc and the chord in the contact zone gives the slip length $u \cong \frac{a^3}{3R^2} \cong 0.03$ mm. At a vehicle velocity $V = 30$ m.s^{-1} (around 110 km/h), the contact time of a point on the tread can be estimated by the relation $t_c = 2a/V$, which is of the order of $t_c \approx 10^{-3}$ s. The order of magnitude of the slipping velocity is then $v_s \approx u/\ t_c$, which gives $v_s \approx 3\times 10^{-2}$ m.s^{-1}. Another key feature is that, for a travelling vehicle, contacts occur in open-cycle conditions, meaning wear particles are (at least in part) eliminated from the countersurface within the contact zone.

The three primary mechanisms which have been proposed for rubber abrasion are abrasive wear, fatigue wear, and smear wear [7,8]. One evidence of the distinct mechanisms contributing to wear originates from the observation of (at least) two distinct types of wear debris [5,9]. The first type consists in material fragments which have been teared away from the sample by fracture/tearing mechanisms [10,11]. These fragments have a broad distribution of sizes, from typically 100 nm up to tens of micrometers. The second type is the so-called smear wear, which gives rise to a sticky layer deposited on the sample surface, in which the architecture of the material seems to be degraded down to the molecular level [12–14]. Filler particles may significantly affect the associated physical-chemical degradation mechanisms, depending on the nature of their surface [13].

The objective of this paper is to go a step further into the elucidation of wear mechanisms under very low severity wear conditions. Wear tests have been performed using the device mentioned above, under well-controlled conditions. The resulting wear patterns and surfaces have been carefully analyzed with advanced physico-chemical characterization techniques. As the nature of reinforcing filler particles may affect chemical processes associated to degradation, materials with two different types of nanofillers, namely carbon black and precipitated silica, were tested.

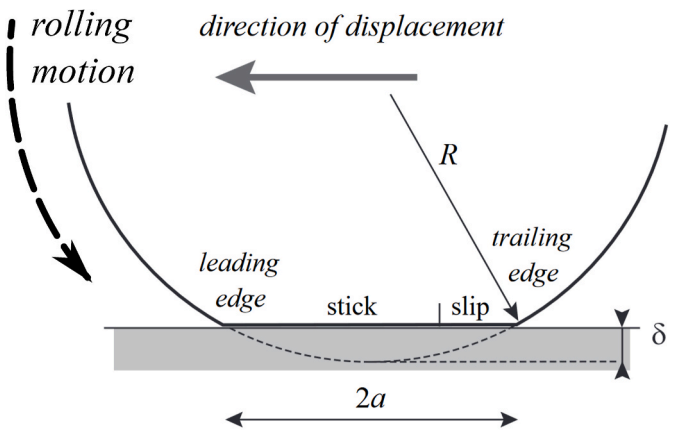

Fig. 1. Schematics of the contact zone of a tire tread. Slip occurs at the trailing edge of the contact zone when the ratio of tangential to normal stress exceeds the friction coefficient, μ [4].

2. Materials and methods

2.1. Materials

The studied materials are synthetic rubber materials representative of tire tread materials reinforced either with carbon black fillers (N234, sample C1) or highly dispersible precipitated silica manufactured by Solvay (Zeosil® 1165 MP, sample S1 and ZP200, sample S2), as reported in Table 1. N234 has a specific surface of approximately 120 m^2/g while Z1165 has around 160 m^2/g and ZP200 has 200 m^2/g. Triethoxysilylpropyltetrasulfur (TESPT) was used as coupling agent for silica-reinforced samples to create covalent bonds between the fillers and the matrix. Other components are additives such as stabilizers, vulcanization activators, and accelerators commonly used in rubber formulations.

The matrices are blends of Styrene Butadiene Rubber (SBR) and Butadiene Rubber (BR), using two different grades of SBR with varying glass transition temperatures (T_g). The characteristics of the two grades are presented in Table 2. Samples were processed at Solvay (Collonges au Mont d'Or, France) in an internal mixer (Bradender 380 cm^3). Sulfur vulcanization was performed at 150 °C under a pressure of 180 bar. The curing times in the press (45 min for S1, 30 min for S2 and 20 min for C1) were adapted to the vulcanization kinetics of the samples, as measured by a Monsanto R100 Oscillating Disc Rheometer at 150 °C.

2.2. Mechanical behavior

Wear resistance must be somehow related to the mechanical properties of the materials. Therefore, a comprehensive characterization of these properties has been performed in the linear and non-linear regimes.

The storage (G') and loss (G'') shear moduli were measured at 40 °C using oscillatory shear at a frequency of 10 Hz, with dynamic amplitudes ranging from 0.1 % to 50 %. These measurements were conducted using a Metravib Dynamic Mechanical Analyzer (DMA). The results are presented in Fig. 2.

As commonly observed, the moduli at small amplitudes and the amplitudes of the Payne effect ($\Delta G'$) are substantially higher in the carbon black-reinforced sample (C1) than in silica-reinforced samples (S1 and S2) [15,16]. Nevertheless, the samples S1 and C1, with the same SBR grade, display comparable storage modulus (G') values at 50 % amplitude. When comparing the two silica-reinforced samples, S1 exhibits a slightly lower storage modulus at low amplitudes and a higher Payne effect.

Table 1
Formulations of the S1, S2 and C1 studied materials. Units are in phr (grams per hundred grams of rubber).

	Components	S1	S2	C1
Matrix	SBR_1	82.6	_	82.6
	SBR_2	_	70	_
	BR	30	30	30
Fillers	Z1165	80	_	_
	ZP200	_	60	_
	CB N326	6	6	6
	CB N234	_	_	80
Additives	TESPT	6.4	6	_
	Oil TDAE	7	_	7
	Stearic acid	2	2	2
	ZnO	2.5	2.5	2.5
	6PPD[a]	2	2	2
	Sulfur	1	1	1
	CBS[bb]	2	2	2
	DPG[cc]	1.5	1.5	1.5
	Filler volume fraction	0.25	0.23	0.26

[a] 6PPD: N-(1,3-dimethylbutyl)-N′-phenyl-P-phenylenediamine (antioxidant).
[b] CBS: N-cyclohexyl-2-benzothiazolesulfenamide (primary accelerator).
[c] DPG: N,N′-Diphenyl guanidine (secondary accelerator).

Table 2
Characteristics of SBR grades.

Reference	Vinyl (%wt)	Styrene (%)	Oil (type/phr)	Tg (°C)
SBR_1	44.5	26	TDAE/37.5	−29
SBR_2	9	25	No	−69

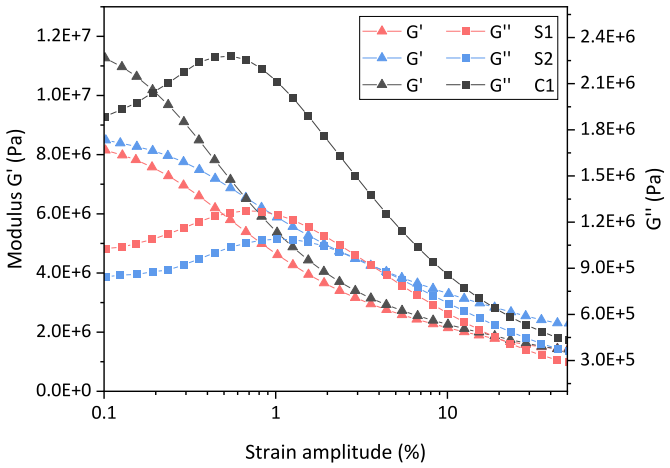

Fig. 2. Storage (G', squares) and loss (G'', triangles) shear moduli as a function of the strain amplitude. Results were obtained at 10 Hz and T = 40 °C for samples S1 (SBR_1 filled with silica Z1165), S2 (SBR_2 filled with silica ZP200) and C1 (SBR_1 filled with carbon black).

Tensile tests were performed at room temperature using the single-column INSTRON 68SC-5 tensile machine, with a constant displacement rate of 500 mm/min, corresponding to a nominal strain rate $\dot{\lambda} = 0.4\ s^{-1}$. The nominal stress-strain curves, shown in Fig. 3, represent the average results of five different tests per materials.

Samples S1 and C1, which have the same SBR grade but differ in filler type, behave similarly at low strain amplitudes. However, the carbon black-reinforced sample (C1) exhibits a higher elongation at break. Additionally, there are noticeable differences between the two silica-filled samples. Sample S2 shows a higher stress at break as compared to sample S1, along with a slightly lower elongation at break. These differences are attributed to the presence of oil in the S1 formulation.

It has been established that friction and wear of elastomers are affected by the visco-elastic response of the materials, that is, by the distance to the glass transition temperature T_g [17–19]. Thus, dynamic mechanical analysis at small amplitudes was also performed using a Mettler Toledo DMA 1. Storage (E') and loss (E'') oscillatory tensile moduli are plotted as a function of temperature (from −80 °C to 60 °C) in Fig. 4, for the three studied materials. The tests were conducted at 10 Hz with a temperature ramp of 3 °C/min and a strain amplitude of 0.12 %. The curves highlight the T_g difference between the two different grades of SBR. Sample S2 (SBR_2) has a lower T_α ($T_\alpha = -70$ °C, measured from the maximum of E'') as compared to the other samples (SBR_1; $T_\alpha = -38$ °C for C1, $T_\alpha = -37$ °C for S1). Additionally, the storage modulus at small amplitude is slightly higher for the carbon black-reinforced sample, as previously observed in Fig. 2.

2.3. Characterization techniques

Two different scanning electron microscopes (SEM) were used. Debris were observed with a MIRA3 FEG SEM from TESCAN, while edge images of the samples were obtained with a Quanta FEG 250 SEM from Thermo Fisher.

X-ray Photoelectron Spectroscopy (XPS) was used to analyze the debris and characterize the worn surfaces. This non-destructive technique makes use of the photoelectric effect, where electrons are emitted from atoms in response to incident electromagnetic radiation. For a kinetic energy of 1385 eV associated with the electron transition in the 2p silicon orbital, the inelastic mean free path is $\lambda \approx 2$ nm, corresponding to a probing depth of about 6 nm. Therefore, the XPS is particularly effective for analyzing surface chemical changes. Measurements were conducted using an Ulvac-PHI Versaprobe III system, featuring a monochromatized Al Kα X-ray source ($h\nu = 1486.68$ eV, wavelength $\lambda = 0.834$ nm). The X-ray beam had a spot size of 200 µm. Survey scans were recorded over a wide energy range (0–1260 eV) at a pass energy of 224 eV and high-resolution spectra of regions featuring the C 1s, Si 2p and S 2p transitions were obtained using a pass energy of 24 eV with a double beam charge compensation system (ions and electrons). Spectral fitting was performed using CasaXPS software using pseudo-Voigt lineshapes with a Shirley background. The C–C bond contribution of the C 1s peak

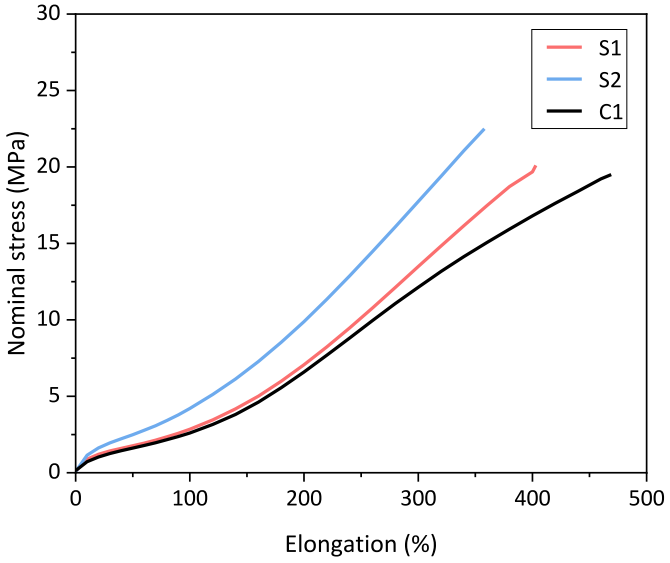

Fig. 3. Nominal stress as a function of the elongation up to tensile failure, measured at room temperature with a ramp rate of 500 mm/min for samples S1 (SBR_1 filled with silica Z1165), S2 (SBR_2 filled with silica ZP200), and C1 (SBR_1 filled with carbon black).

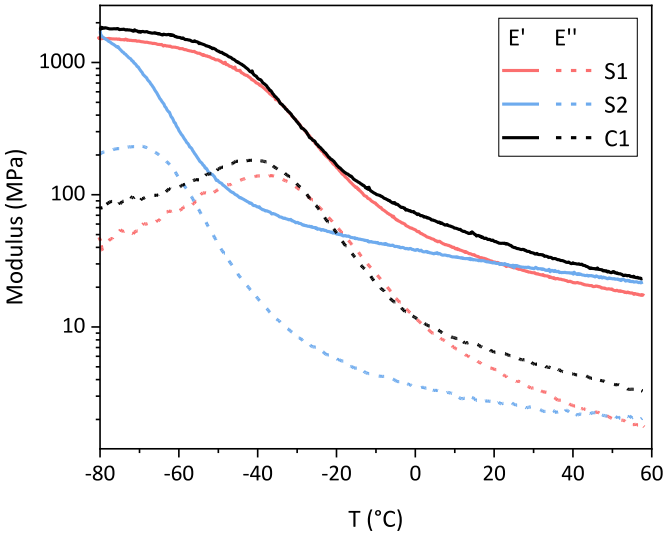

Fig. 4. Storage (E', continuous lines) and loss (E'', dotted lines) tensile moduli as a function of the temperature (from −80 °C to 60 °C) in the linear regime (amplitude 0.12 %, frequency 10 Hz), for samples S1 (SBR_1 filled with silica Z1165), S2 (SBR_2 filled with silica ZP200) and C1 (SBR_1 filled with carbon black).

was calibrated to 284.8 eV to correct for any remaining charge effects. Surfaces were cleaned with ethanol prior to characterization. Quantification was performed using relative sensitivity factors from Wagner et al. integrating a correction for the penetration depth of the analysis [20]. An angular distribution correction was also applied using the transmission function to account for the 45° angle between the X-ray source and the axis of the analyzer.

2.4. Tribometer

Abrasion tests were conducted using a custom-built tribometer [21]. This device includes a piezoelectric dynamic actuator that intermittently presses the sample against a rotating abrading disk with a controlled force. It has been designed to meet two main requirements. First, it simulates dynamic sliding contacts in conditions modeling the local sliding experienced by real tires in low severity usage conditions (straight line, constant speed). Second, it allows performing accelerated wear tests, that is, accumulating a large sliding distance within a short time.

The tribometer enables independent control of the contact frequency, normal force and sliding velocity. In addition, the tribometer works in open-cycle condition, allowing wear debris to be periodically removed from the contact zone. This is an essential feature when comparing to real usage. It was shown that the cleaning periodicity has an impact on the wear rate [5]. The abrading disk (MICROPLAN FRANCE) is composed of granite (granite bleu de Guéret). Its chemical composition primarily includes SiO_2 (~65 %), Al_2O_3 (~15 %), Na_2O and K_2O (~7 %) and other metal oxides (Fe, Mg, Ca) [22]. It was selected to provide a counter-surface with a composition similar to that of roads, while ensuring a constant roughness throughout the wear test [5]. The topography of the surface was characterized with a Surfascan tactile profilometer. The 2D profiles in the wear track were obtained over a length of 4.8 mm and at a speed of 0.3 mm s^{-1} perpendicular to the sliding direction, after cleaning the surface. The roughness indicators were then calculated using a 0.8 mm wavelength filter in accordance with ISO 21920 and averaged over 10 measurements. The measured indicators are $\langle R_a \rangle = 0.95 \pm 0.33$ µm et $\langle R_t \rangle = 13.0 \pm 4.3$ µm.

The general architecture of the tribometer is schematized in Fig. 5. It is fully controlled by a LabVIEW software. The abrading disk rotates around the vertical axis z with an angular velocity ω, resulting in a sliding velocity $v_s = R\omega$ with R the distance between the disk axis and the sample. For all tests presented here, R was fixed at 102.5 mm. The piezoelectric actuator allows applying intermittent contacts between the sample, which is glued on the sample holder, and the disk. This actuator acts along the z axis and controls the frequency and duration of contacts as well as the normal force with a fast force-controlled loop. Normal (z axis) and tangential (x axis) forces are measured during the test with a 3-axis load cell. The heating unit, thermal sensor, and a thermocouple (within the sample holder close to the sample) enable temperature control within the chamber. The tribometer can also be equipped with an infrared camera to measure the surface temperature variations of the sample during the test. Note also that working with small samples is contact with an aluminum sample holder eliminates dissipative self-heating of the sample, thus enabling precise control of the overall sample temperature.

The sample geometry consists of a thin disk with a diameter $D = 18$ mm and a spherical cap with a radius of curvature of 40 mm. This sphere-on-plane geometry provides several advantages. It minimizes border effects and instabilities during contact initiation and tedious alignment procedures (which are required when e.g. a cylinder-on-plane geometry is considered). Additionally, with a maximum sample thickness of $e = 2$ mm ($e \ll D$), it should conform to the conditions of the elastic layer model. This implies that lateral displacements within the sample under a normal force are very small compared to the compressive displacement, leading to a higher effective modulus. Consequently, on such a thin sample, it is possible to apply a pressure much larger than on a semi-infinite sample. Samples were glued to the sample holder using acrylic glue.

2.5. Wear tests procedure

The wear test procedure was designed to perform accelerated wear tests that mimic real conditions and give reproduceable results. The procedure was based on the methodology developed and reported in Ref. [5].

For all presented results, the sliding velocity was fixed to 50 mm s^{-1}. The actuator generates square pulses to compress the sample against the disk with a normal force of 10 N, providing cyclically intermittent slip. The normal force is controlled through a fast closed-loop system. All experiments were performed at room temperature. The sliding velocity and the applied normal force were selected to align with the orders of magnitude observed under real tire-road conditions, as described in the introduction. The general test procedure is detailed below.

Before starting a wear test, the test sample is glued to the sample holder and weighted. A "reference sample", identical to the test sample, is prepared in the same manner and placed under identical conditions but is not worn. It is used to measure relative mass losses, thereby minimizing the influence of environmental factors (such as water uptake).

A wear test consists of several wear periods. Each wear period involves a series of N_c contacts (Fig. 6a). Each contact comprises 1 s of contact time followed by 0.1 s of non-contact (relaxation) (Fig. 6b).

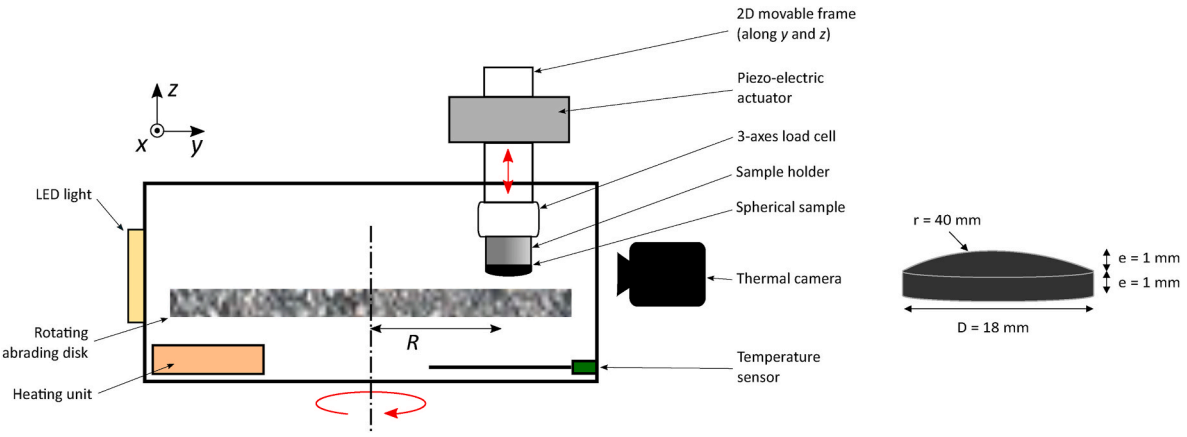

Fig. 5. Schematics of the general architecture of the rotary tribometer and sample geometry (sphere-on-plane). The camera is an infrared camera for local temperature measurements.

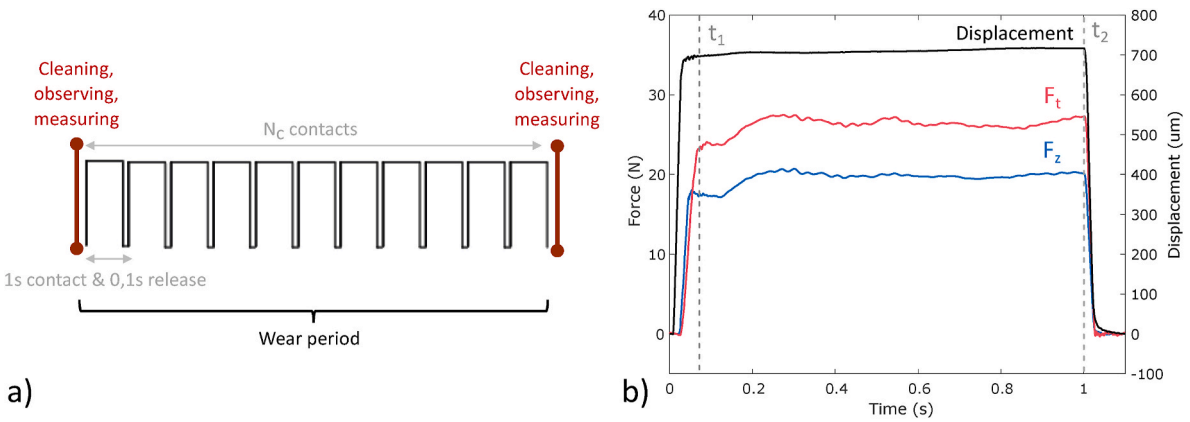

Fig. 6. Schematics of one wear period of N_c contacts (a); Profiles of the displacement, normal (F_Z) and tangential (F_t) forces during a single contact (b). Full sliding occurs between t_1 and t_2.

Fig. 6b illustrates the dynamics of loading within a contact between the sample and the disk during the wear test. First, the actuator takes approximately 25 ms to compress the sample on the disk surface up to the targeted value of the normal force F_Z. Concomitantly, the sample is sheared due to the sliding velocity, which leads to an increase in the tangential force F_t until it stabilizes when global sliding over the whole contact zone is established (Fig. 6b). In our test conditions, with a constant sliding velocity $v_S = 50$ mm.s^{-1}, the time to reach this steady state averages to 0.07 s. The corresponding time t_1 defines the onset of full sliding (Fig. 6b).

A point on the tire tread is periodically subjected to stress at a frequency of approximately 10 Hz. It is here hypothesized that the test remains representative of real conditions by maintaining a frequency close to 1 Hz. Imposing a frequency of 10 Hz on the tribometer would reduce the result reproducibility, as the time required for the piezoelectric actuator to regulate the force would become comparable to the contact time. Furthermore, the fraction of contact and non-contact time was selected to maximize the contact duration while allowing the material to relax. This approach enables accumulating a large slip length within a relatively short period of time.

After each wear period of N_c contacts, debris are removed from the abrading disk, first physically using an eraser (STAEDTLER Mars plastic) and then chemically with ethanol and acetone. The surfaces of both the worn and reference samples are also cleaned with ethanol. After this step, samples are weighed together with sample holders, and the wear pattern is observed. The test sample is then reloaded into the tribometer for the next period. This process is repeated for a total of 10 wear periods.

Wear is quantified by the weight loss of the sample during the test. After each wear period i (with $i = 1, 2, \ldots, 10$), both the worn sample (m_{sample}) and the reference sample (m_{ref}) are weighted after cleaning. The weight of wear debris generated during the i^{th} wear period ($\Delta m_{sample}(i)$) is calculated as:

$$\Delta m_{sample}(i) = \left[m_{sample}(i-1) - m_{sample}(i)\right] - \left[m_{ref}(i-1) - m_{ref}(i)\right]$$

The total accumulated weight loss after n_w wear period ($\Delta m_{tot}(n)$) is then:

$$\Delta m_{tot}(n_w) = \sum_{i=1}^{n_w} \Delta m_{sample}(i)$$

The number N_c of contacts in each wear period determines the cleaning frequency, which influences the wear rate. The impact of this parameter was discussed by Huang et al. [5]. In this study, it was decided to carry out $N_c = 500$ contacts per wear period. A wear test is thus composed of 10 wear periods of 500 contacts which last 1.1 s (1 s of contact and 0.1 s of non-contact). The sliding distance during a single wear period is thus approximatively 500 × 50 mm, that is 25 m and the overall wear test (10 wear periods) gives an accumulated slipped length of 250 m. Assuming that a point on the tire slides over a length of 0.03 mm each time it comes into contact with the road, as mentioned in the Introduction, the test would simulate about 8×10^6 contacts, which corresponds to around 15 000 driven kilometers.

During the j^{th} contact, the frictional energy $E(j)$ is calculated as the work of the tangential force:

$$E(j) = v_S \int_{t_1}^{t_2} F_t(t)dt$$

Where $t_1 = 0.068$ s and $t_2 = 1$ s define the sliding contact duration. The accumulated frictional energy during the i^{th} wear period E_i is given by (where the sum is over the N_c contacts of period i):

$$E_i(N_c) = \sum_{j=1}^{N_c} E(j)$$

The total accumulated frictional energy E_{tot} after n_w wear periods is then calculated as:

$$E_{tot}(n_w) = \sum_{i=1}^{n_w} E_i(N)$$

The wear rate of a material during a wear test is typically described by the weight or volume loss per unit sliding length or per unit frictional energy [23]. By plotting the total weight loss as a function of accumulated friction energy for each wear period, $\Delta m_{tot}(n) = f(E_{tot}(n))$, linear relationships are obtained, with slopes representing the wear rate [5]. Furthermore, both quantities $\Delta m_{tot}(n)$ and $E_{tot}(n)$ scale proportional to the contact area. Since the real contact area is not quantitatively measured and the contact pressure is non-uniform across the contact surface, this definition of the wear rate circumvents the necessity to account for the contact area, which may also change along the test or depend on the mechanical response of the particular sample under study.

2.6. Thermal measurements

The infrared camera is a FLIR SC7600 MWIR, with a wavelength range of 2.5–5 μm and equipped with an optical lens of 25 mm focal length. The maximum frame rate is 380 Hz and the noise-equivalent temperature is lower than 25 mK. In this study, the pixel size is 80 × 80 μm^2, and the acquisition frequency was set to 50 Hz. The lens axis of the camera is kept fixed and held perpendicular to the lateral surface of the sample.

An important parameter in infrared thermography is the emissivity

of the material (ε_{sample}), which is defined as the ratio of the radiation intensity emitted by the real object to that emitted by a black body (BB). The latter absorbs all incident radiation, regardless of wavelength or direction, and has an emissivity of $\varepsilon_{BB} = 1$. The emissivity of the sample is measured indirectly through spectral reflectivity [24] and using equation (1).

$$IT_{cam} = \varepsilon_{sample} IT(T_{sample}) + (1 - \varepsilon_{sample}) IT(T_{env}) \quad (1)$$

With IT_{cam} the digital level of the camera, ε_{sample} the sample emissivity and T_{env} the environmental temperature. The method aligns with the approaches presented in Ref. [25]. The black body emits infrared radiation towards the sample surface, and the IR camera captures the reflected radiation. The material emissivity was measured at an incident angle of 30° using three different black body temperatures: 15 °C, 30 °C, and 45 °C.

The obtained emissivity has a mean value of 0.93 ± 0.02 for the studied materials. It is high enough to enable reliable temperature measurements. Moreover, the small standard deviation indicates that the emissivity across the sample may be considered to be homogeneous. However, to avoid any environmental effects, temperature variations rather than absolute temperature values were compared. Since a wear period lasts about 9 min, the environmental temperature can be considered constant, allowing the second term on the right-hand side of equation (1) to be eliminated through the comparative method.

3. Results and discussion

3.1. Wear test results

Wear tests performed on samples S1, S2 and C1 produced the straight lines shown in Fig. 7. Each point on the curve corresponds to one wear period of 500 contacts, as the samples are weighed after each period. Curves contain 10 points as overall wear tests are composed of 10 wear periods. The slope of the obtained linear regression represents the wear rate.

Wear results reported in Table 3 are average values obtained on three samples. The obtained low standard deviations highlight the good reproducibility of the test. The apparent pressure was calculated based on the apparent contact area measured with a digital microscope at the end of the 10 wear periods. The results show that this apparent pressure is slightly higher for sample S2. The apparent (macroscopic) friction factor f_a is defined as $f_a = \overline{F_t}/\overline{F_z}$ where $\overline{F_t}$ and $\overline{F_z}$ are the averages of the tangential and normal forces recorded throughout the entire test when full sliding occurs during contact, i.e. between t_1 and t_2 (as defined in Fig. 6b):

$$\overline{F_t} = \frac{1}{n_w N_c (t_2 - t_1)} \sum_{i=1}^{n_w} \sum_{j=1}^{N_c} \int_{t_1}^{t_2} F_t(t) dt$$

The apparent friction factor remains approximately constant throughout the wear test, with slightly different mean values observed for the three materials.

The measured wear rates range from 0.1 to 0.3 mg/kJ, corresponding to average abraded heights of 10–50 µm over the entire wear tests. Results reported in Table 3 indicate that sample S2 exhibits a significantly lower wear rate as compared to the other two samples under the studied conditions. Additionally, it is observed that samples S1 and C1, which share the same matrix but differ in the type of filler (silica or carbon black), display similar wear rates, as evidenced by the overlapping error bars. Therefore, according to these findings, the type of filler appears to have no significant impact on the wear rate as defined and measured in this study.

Note that the fitted linear regressions in Fig. 7 do not always go through the origin, or only in a very approximate way. Indeed, there may exist a transitory period at the beginning of the test (typically during the first wear period) in which the wear may be significantly affected by the initial surface state or rugosity of the samples, and thus may not be fully reproduceable. Accordingly, the origin point $\Delta m_{tot}(0) = 0$ is excluded from the computed linear regressions.

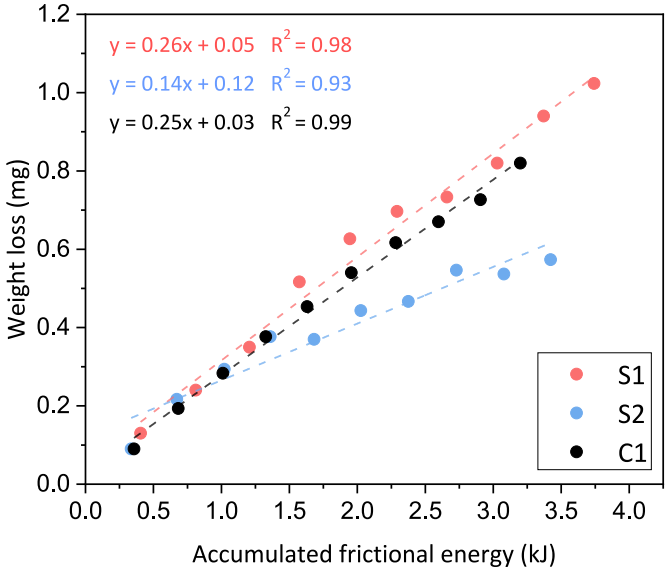

Fig. 7. Weight loss as a function of the accumulated frictional energy for samples S1 (SBR_1 filled with silica Z1165), S2 (SBR_2 filled with silica ZP200) and C1 (SBR_1 filled with carbon black). Each point is obtained at the end of a wear period of 500 contacts. Tests are performed at room temperature under a fixed normal force of 10 N and a sliding velocity $v_S = 50$ mm.s^{-1}.

Table 3
Wear results for the materials studied after 10 wear periods of 500 contacts. Error bars represent the standard deviation, calculated from three tests conducted per sample.

	S1	S2	C1
Average wear rate (mg/kJ)	0.31 ± 0.04	0.17 ± 0.03	0.26 ± 0.02
Average apparent pressure (bar)	3.32 ± 0.03	4.84 ± 0.14	3.34 ± 0.20
Average apparent friction factor f_a	1.73 ± 0.13	1.37 ± 0.12	1.33 ± 0.13

3.2. XPS analysis

To investigate whether chemical changes occur on the surface of the samples during wear, worn surfaces were analyzed using XPS. Peaks associated to carbon, oxygen, zinc, calcium, sulfur, and silicon were observed in the survey spectra of all samples. The XPS survey spectrum of sample S1 is shown in Fig. 8 and the corresponding spectrum data are reported in Table 4.

Samples mainly contain carbon (89 %) from the elastomer matrix and oxygen (≈ 9 %) from fillers, additives (e.g., ZnO) and possible surface contamination. The vulcanization additives and fillers are detected in minor quantities (< 3 %). It is observed that the peaks of both sulfur and silicon are influenced by wear. Therefore, the following analysis will focus on these peaks. The obtained high-resolution spectra are slightly noisy, as the detected quantities are very small. Carbon spectra were not selected because the results obtained in the different regions (unworn and worn) were similar (spectra are presented in the supplementary information). Additionally, the abundance of C-C bonds in the sample makes fitting the other carbon bonds highly imprecise.

3.3. Sulfur oxidation due to wear mechanism

Fig. 9 shows the high-resolution spectra of the S 2p core levels recorded from sample C1 after the whole wear test, either in the unworn

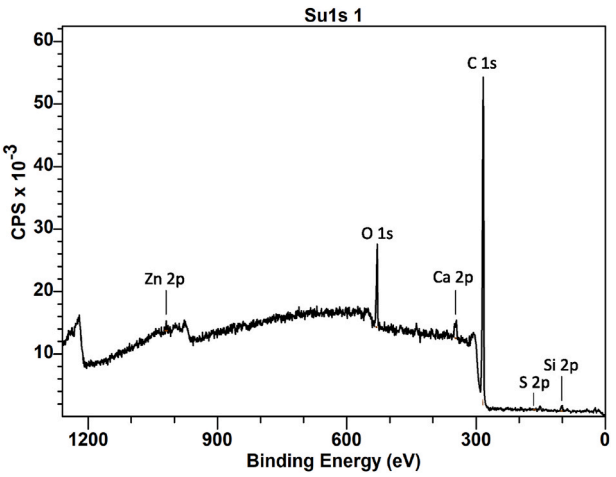

Fig. 8. XPS survey spectra recorded from the unworn surface of sample S1 (SBR_1 filled with silica Z1165). High-resolution analyses will then be focused on sulfur (S) and silicon (Si), in the range 90–180 eV.

Table 4
XPS survey spectrum data referring to Fig. 8. The atomic concentration refers to the relative number of each atom over the total number of detected atoms.

Sample	Element / Transition	Peak energy (eV)	Atomic concentration (at%)
S1 – unworn area	O 1s	532	8.7
	C 1s	286	89.0
	Zn 2p	1022	0.1
	Ca 2p	348	1.0
	S 2p	163	0.1
	Si 2p	102	1.2

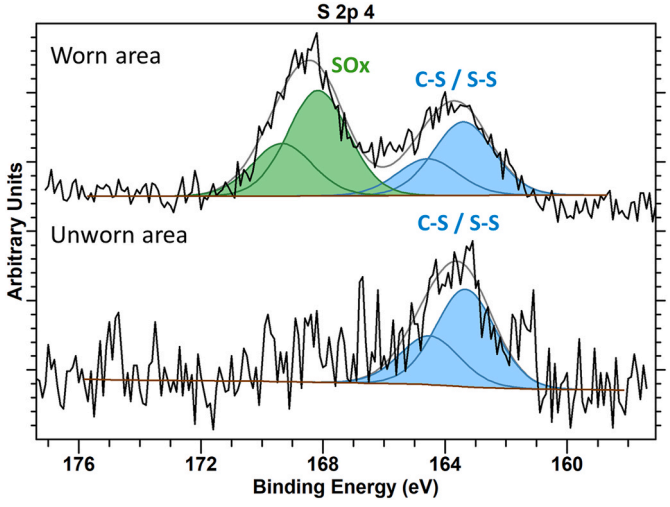

Fig. 9. XPS spectra and fits of S 2p peaks carried out on sample C1 obtained in worn and unworn areas.

or worn region. Fitting details are provided in Table 5. For all tables related to XPS fitting of high-resolution spectra, atomic concentrations are expressed as a percentage of the total number of detected atoms for the element in question.

For sulfur 2p orbitals, core level ionization causes spin-orbit splitting resulting in a two-peak signal called doublet with area ratios ½ and peak separation of 1.18 eV. All S 2p spectra were thus fitted accordingly. In the unworn area, only one contribution is observed in the sulfur region, appearing as a doublet at 163.3 and 164.5 eV (in blue). This doublet is assigned to a chemical environment of C-S or S-S bonds [26]. The same analysis was performed within the wear pattern. Two distinct contributions are now observed: the original doublet around 163 eV remains present, while a new doublet at higher binding energy around 168 eV distinctly appears. It is compatible with an oxidized sulfur chemical environment (in green) [26]. Similar results were observed for samples S1 and S2 containing silica particles (corresponding spectra are shown in Figs. 10 and 16). This indicates that the phenomenon is independent of the type of filler. The antioxidant function of carbon black, which acts as a radical scavenger, does not seem to prevent the oxidation of sulfur [27,28].

These results suggest that sulfur oxidation occurs due to wear. However, related to the processing conditions, there may possibly exist some initial difference or a gradient in chemical composition between the surface and the bulk of the sample, and wear might simply reveal this difference as it erases a surface layer of thickness of order 50 µm. To test this hypothesis, a 80 µm slice was removed from the sample outer surface with a razor blade for bulk analysis. Fig. 10 shows the S 2p spectra for sample S2 as a representative example obtained in the wear pattern and in the cut area (bulk of the sample) with information in Table 6. In the bulk material, only the doublet around 163 eV is observed, similar to the signal from the unworn surface. This demonstrates that the presence of oxidized sulfur is indeed associated to a chemical reaction occurring on the surface of the material during wear, rather than to a potential skin effect.

Comparing different formulations to quantitatively determine which

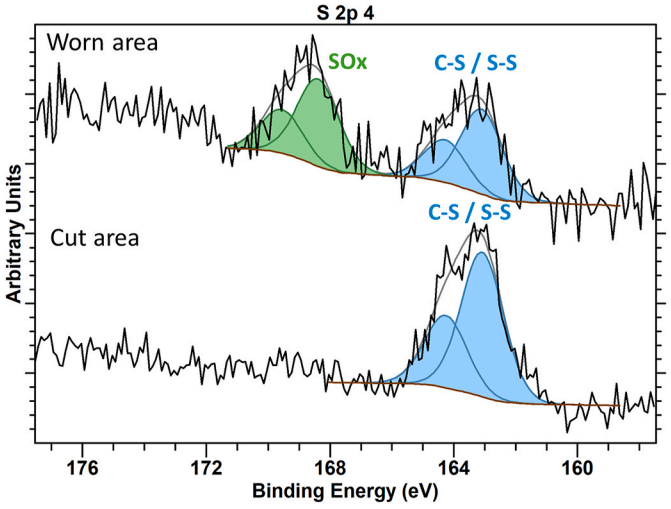

Fig. 10. XPS curve fitting of the S 2p peak carried out on sample S2, obtained from the worn and cut areas.

Table 5
Parameters obtained by fitting the XPS peaks associated to S 2p with doublets of pseudo-Voigt functions (see text) in sample C1 on both worn and unworn areas.

Sample Id	Element / Transition	Peak energy (eV)	FWHM (eV)	Percentage of total sulfur (at%)	Assignment
C1 – Worn area	S $2p_{3/2}$-S $2p_{1/2}$	163.4–164.6	2.3	43	C-S/S-S
	S $2p_{3/2}$-S $2p_{1/2}$	168.2–169.3	2.3	57	SOx
C1 – Unworn area	S $2p_{3/2}$-S $2p_{1/2}$	163.3–164.5	2.3	100	C-S/S-S

Table 6
Parameters obtained by fitting the XPS peaks associated to S 2p with doublets of pseudo-Voigt functions (see text) in sample S2 from both the worn and cut areas.

Sample Id	Element / Transition	Peak energy (eV)	FWHM (eV)	Percentage of total sulfur (at%)	Assignment
S2 – Wear pattern	S $2p_{3/2}$-S $2p_{1/2}$	163.1–164.3	1.6	50	C-S/S-S
	S $2p_{3/2}$-S $2p_{1/2}$	168.4–169.6	1.6	50	SOx
S2 – Cutting area	S $2p_{3/2}$-S $2p_{1/2}$	163.0–164.3	1.6	100	C-S/S-S

one oxidizes more is challenging due to the high measurement noise, which is related to the very small quantities being measured. Consequently, XPS observations are used primarily to detect the presence or absence of specific bonds rather than to quantify oxidation levels. The relative values of peaks areas, however, indicate that a significant fraction (typically a few tens of percent) of oxidized S atoms is detected in the worn area.

As already mentioned about smear wear [14], the wear mechanism envisaged in these conditions is the breaking of C-S or S-S bonds, which have lower energy than C-C bonds [29], leading to the formation of sulfur free radicals on the surface that subsequently react with atmospheric oxygen [9,30].

An important question is whether these bond scissions result from mechanical phenomena associated with abrasion wear or from local thermal phenomena. To help discriminating this question, an infrared camera was installed to monitor the temperature changes of the sample during the wear tests. The results are discussed in the next section.

3.4. Thermal analysis

When rubber slips on a hard, rough substrate, the substrate asperities induce time-dependent deformations on the rubber surface. This results in viscoelastic energy dissipation within the rubber, leading to friction and to localized heating [31]. The term *flash temperature* denotes the localized and short duration temperature increase within the sliding contact. Estimating and measuring the local temperature is important in our study, as it has been argued that local heating can be significant for sliding velocities of the order of 10^{-2} m.s^{-1} [31].

In the tribometer, the thin sample is glued on an aluminium sample holder, which is screwed into a thermally conductive assembly. This enables efficient heat dissipation from the sample, ensuring that the tests are conducted under isothermal conditions, as already mentioned in Section 2.4. This contrasts with full-scale tests, where the temperature field within the sample may be poorly controlled due to self-heating associated with bulk viscoelastic dissipation. Here, the measured temperature rise corresponds solely to the local temperature increase generated in the vicinity of the contact surface by friction.

First, the theoretical flash temperature was estimated using equation (2) [32,33].

$$\Delta T = \frac{f F_z v_S}{A}\left(\frac{\lambda_1}{L_1}+\frac{\lambda_2}{L_2}\right)^{-1} \quad (2)$$

Where f is the friction factor, F_z is the normal force, v_S is the sliding velocity, A is the real contact area, taken to a first approximation as the apparent contact area $A = \pi a^2$ (a is the contact radius), $\lambda_1 \cong 0.2$ W/mK [34] and $\lambda_2 \cong 3.5$ W/mK [35] are the thermal conductivities of the elastomer and granite, respectively. L_1 et L_2 are characteristic dimensions associated to the contact: $L_1 = \pi a/4$ and $L_2 = 0.31\pi a/\sqrt{Pe}$ where $Pe = a v_s \rho_2 c_2/\lambda_2$ is the Péclet number. Here, $\rho_2 \cong 2.7\times 10^3$ kg/m^3 [35] is the density of granite and $c_2 \cong 886$ J.kg^{-1}.K^{-1} [36] is the specific mass heat capacity of granite.

The calculated theoretical temperature increases are shown in Table 7. Under the applied test conditions, the maximum temperature rise of the samples in the contact is estimated to be less than 3 °C.

Flash temperatures are challenging to measure in practice. Thermal measurements were conducted on the sample surface with a resolution of 80 μm^2 (corresponding to the camera pixel size) to estimate the maximum temperature variation at this scale, which roughly corresponds to the scale of the wear debris. Thermography measurements were performed and analyzed as described in the Experimental Section, using a sample emissivity value of 0.93. Fig. 11 shows a representative thermal image of sample S1, during the last wear cycle. The temperature rise is higher at the rear than at the front of the contact, in the compression zone. It is also at the rear of the contact zone that the wear is more pronounced when observing the wear patterns.

Table 7
Comparison of temperature deviations ΔT for samples S1, S2 and C1 during the wear test, measured by an infrared camera during the last wear cycle and calculated with the theoretical formula, equation (2).

	S1	S2	C1
Theoretical ΔT (°C)	2.4	2.5	1.9
Experimental ΔT (°C)	1.8	1.7	1.5

Real time IR measurements were processed with a marker-tracking method, to suppress sample displacement and track the thermal evolution of a defined area. The monitored zone was located on the sample and included the contact area with the disk. It is represented by a black rectangle in Fig. 11. The temperature variations were measured from the maximum values within the monitored zone. The thermal variations measured in this zone during the last wear cycle are reported in Table 7. These results are consistent along all successive wear periods, with variations within ±0.5 °C.

Both theoretical and experimental results consistently show that the temperature rise in the contact during wear under the investigated conditions is measurable but very small in any case, on the order of or less than 3 °C. This suggests that the thermal effects on material properties are minor and can be neglected. Therefore, it is probably not temperature that activates the detected chemical reactions, but rather the mechanical phenomena associated with interface shear.

3.5. Silica concentration gradient

Changes were also detected in the XPS peaks associated to silicium in the worn area, and these changes must be elucidated. Fig. 12 shows the high-resolution XPS spectra of the Si 2p core levels recorded from sample S2 at the end of the whole wear test. The fitting details are provided in Table 8.

In the unworn area, only one contribution is observed at 102.1 eV (in

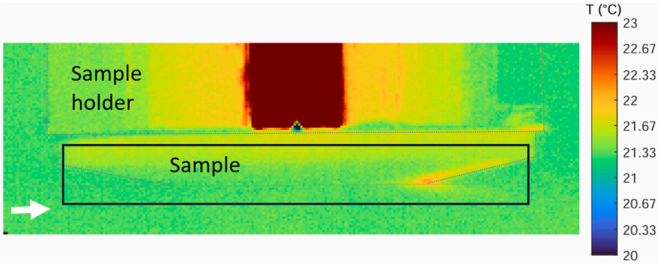

Fig. 11. Image of the thermal measurement of sample S1 during the last wear period. The white arrow indicates the relative displacement of the abrading surface (the sliding direction), and the black rectangle represents the monitored zone used to measure the temperature variations.

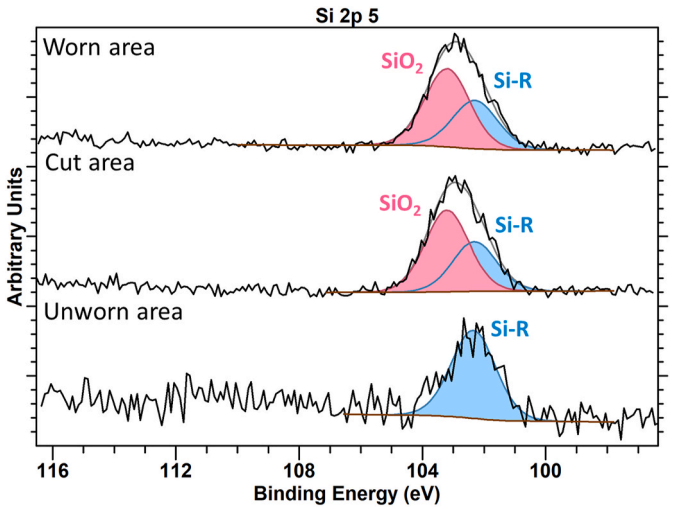

Fig. 12. XPS analyses (Si 2p) carried out on sample S2 obtained on the worn, the cut and the unworn areas.

blue), which is assigned to Si-R bonds [26]. These bonds are present in low concentrations (around 1 % of total detected atoms in silica reinforced samples) and may be attributed to TESPT bonds and possibly to surface contamination. Analysis of the worn surface (Fig. 11) reveals two contributions: the original one at 102.1 eV and a new one at 103.1 eV, attributed to silica (O-Si-O bonds, in pink) [37]. The same result is observed on sample S1, suggesting that silica fillers are not initially present on the extreme surface of the samples but become visible on the surface during wear.

Three hypotheses can be postulated from these observations. First, a silica concentration gradient may exist within the samples, characterized by a surface layer depleted in silica, possibly due to the manufacturing process. Secondly, a reaction involving *SiOH* bonds (silanols) may occur during wear to form SiO_2. Finally, there may be a transfer of abraded granite particles onto the specimens during wear testing.

To gain a deeper understanding of the involved phenomena, analyses were carried out in a cut zone of the sample to investigate the bulk underneath the outer surface, in the same way as it was done previously. The high-resolution spectrum in the Si 2p regions in the cut area is shown in Fig. 12 (curve in the middle of the graph). The observed contributions are consistent with those identified in the wear pattern. This result indicates that the presence of silica cannot be attributed to a chemical reaction induced by the wear mechanism, neither to granite transfer. Therefore, the most plausible explanation for these findings is the presence of a silica-depleted layer at the initial outer surface of the samples, related to the manufacturing process.

SEM analysis was performed on silica-filled samples cryofractured perpendicular to the surface to investigate the presence of a silica-depleted skin layer. A Low Vacuum SEM image of a slice from sample S1 is shown in Fig. 13. A skin layer without silica particles is indeed observed. The thickness of this layer is approximately 100–150 nm, which is nearly twice the size of silica aggregates. As mentioned above, XPS measurements probe the surface to a depth of about 6 nm, which locates the analyzed region well within the silica-depleted layer. However, in the context of wear tests, the silica-depleted layer is extremely thin relative to the overall average abraded depth and is removed during the first wear period. Silica aggregates then flush the worn surface.

3.6. Wear debris analysis

Oxidation phenomena due to wear has already been observed on sticky debris using Energy Dispersive X-ray spectroscopy (EDX) [14]. The authors also noted that the average molecular weight of the sticky debris is lower than that of the original rubber and that debris are soluble in toluene. These findings, together with results from double quantum-proton NMR spectroscopy, suggest that both rubber chains and crosslinks can break during wear.

To supplement these results, XPS analysis was also performed on the wear debris, with slight modifications to the wear conditions. A normal force of 20 N was applied, and debris were collected after only three wear periods of 500 contacts. The increase of the normal force enabled the accumulation of a larger quantity of debris, thereby improving the quality of XPS data. The wear debris were collected using a double-sided carbon tape directly applied to the wear pattern. To ensure that the adhesive on the tape did not interfere with the spectra of the debris, the glue was also analyzed by XPS.

Figs. 14 and 15 show SEM images of the debris from samples S1 and S2, respectively, after three wear periods of 500 contacts. A comparison of the debris reveals significant differences in both size and morphology. Debris from sample S1 are mostly material agglomerates reaching sizes up to 400 µm. In contrast, the debris from sample S2 predominantly consists of rolls and agglomerated rolls, with sizes up to approximately 50 µm. This observation indicates that two distinct mechanisms were involved during the wear of S1 and S2 materials. Despite these differing wear mechanisms and variations in T_g values, the chemical

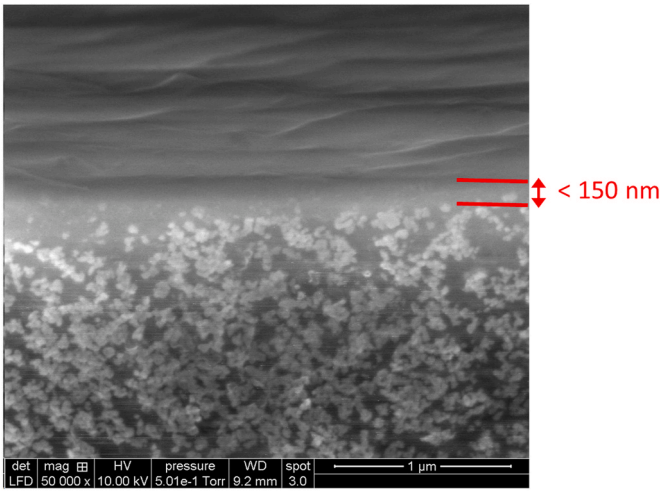

Fig. 13. Low Vacuum SEM image of the unworn sample S1, obtained by cryofracture.

Table 8
Parameters obtained by fitting the XPS signals associated to Si 2p with pseudo-Voigt functions in sample S2 on the worn, the cut and the unworn areas.

Sample Id	Element / Transition	Peak energy (eV)	FWHM (eV)	Percentage of total silicon (at%)	Assignment
S2 – Worn area	Si 2p	102.3	1.7	38	Si-R
	Si 2p	103.2	1.7	62	SiO_2
S2 – Cut area	Si 2p	102.3	1.7	38	Si-R
	Si 2p	103.2	1.7	62	SiO_2
S2 – Unworn area	Si 2p	102.3	1.7	100	Si-R

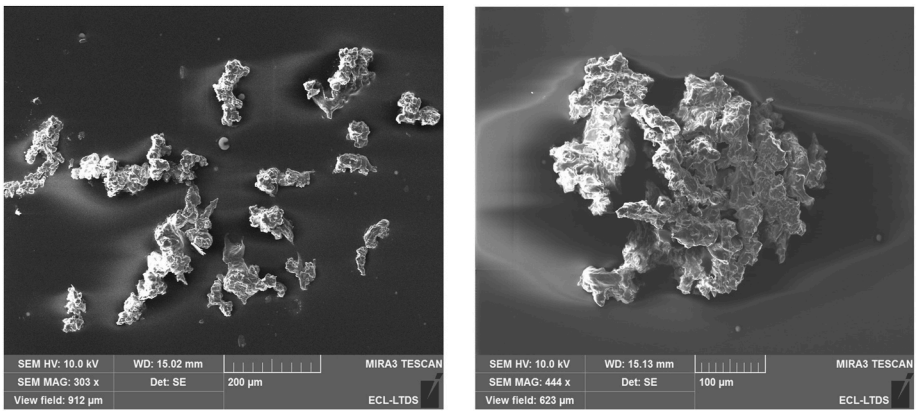

Fig. 14. SEM debris images of sample S1 after thee wear periods ($F_N = 20$ N, $v_S = 50$ mm.s^{-1}, room temperature).

Fig. 15. SEM debris images of sample S2 after thee wear periods ($F_N = 20$ N, $v_S = 50$ mm.s^{-1}, room temperature).

modifications identified by the XPS results remain consistent across both materials. The chemical elements detected in the XPS survey spectra from the analyzed areas of wear debris indicate that debris are primarily composed of rubber material (XPS survey spectra of sample S1 is presented in the Supplementary Information file). Some particles with shape and chemical composition different from wear debris are sometimes observed (see Fig. 15). Those may have been transferred from granite or may come from environmental pollution. However, they are present in small quantities and do not seem to influence the XPS analyses.

High-resolution spectra for the S 2p and Si 2p regions were recorded and analyzed for both the wear pattern and debris from sample S1 (Fig. 16 and Table 9). The spectral features are consistent between the wear pattern and the debris, indicating that the wear debris contains oxidized sulfur, as evidenced by the doublet around 169 eV in the high-resolution S 2p spectrum (green color). Moreover, the presence of silica particles in the wear debris is confirmed by the peak at 103.5 eV in the high-resolution Si 2p spectrum (pink color). The same observations were made on the debris from sample S2. However, the debris from this second formulation are significantly smaller than that from S1, resulting in slightly lower signal-to-noise ratio in the S 2p and Si 2p spectra. Thus, in one of the three debris zones analyzed by XPS for sample S2, sulfur oxidation was not detected in the high-resolution S 2p spectrum, probably due to low signal intensity.

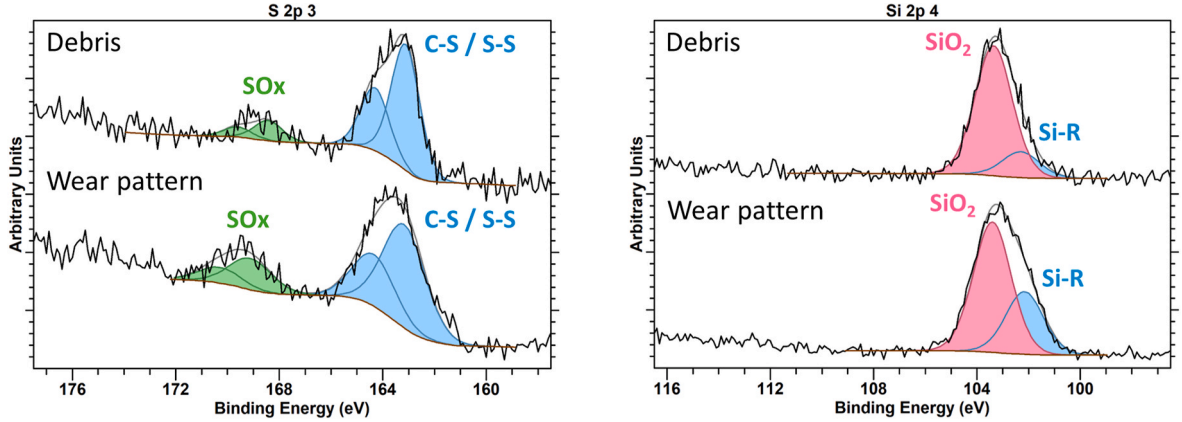

Fig. 16. XPS analyses of the S 2p and Si 2p regions carried out on sample S1. They were obtained on the wear pattern after the whole test process ($F_N = 10$ N) and on debris after thee wear periods ($F_N = 20$ N).

Table 9
Parameters obtained by fitting the XPS spectra associated to S 2p and Si 2p with pseudo-Voigt functions in sample S1 for both debris and wear pattern.

Sample Id	Element / Transition	Peak energy (eV)	FWHM (eV)	Percentage of total sulfur or silicon (in at%)	Assignment
S1 – Debris	S $2p_{3/2}$-S $2p_{1/2}$	163.1–164.3	1.3	75	C-S/S-S
	S $2p_{3/2}$-S $2p_{1/2}$	168.4–169.6	1.3	25	SOx
	Si 2p	102.3	1.7	14	Si-R
	Si 2p	103.3	1.7	86	SiO_2
S1 – Wear pattern	S $2p_{3/2}$-S $2p_{1/2}$	163.2–164.3	1.9	83	C-S/S-S
	S $2p_{3/2}$-S $2p_{1/2}$	169.1–170.3	1.9	17	SOx
	Si 2p	102.2	1.7	33	Si-R
	Si 2p	103.4	1.7	67	SiO_2

4. Conclusion

We have investigated low severity abrasion wear on reinforced elastomer materials representative of tire tread, using a dedicated dynamic tribometer. Three samples with different formulations were investigated. Detailed and systematic XPS analyzes have revealed that low severity wear induces sulfur oxidation on the worn surface of the reinforced elastomers. This mechanism occurs in the presence of both types of fillers investigated, namely precipitated silica and carbon black.

Oxidation phenomena associated to wear in elastomers have already been postulated in several studies. For the first time, we demonstrate the occurrence of such oxidation during low severity wear in a direct way. Besides, we directly demonstrate that it involves sulfur bonds associated to both crosslinks and silica-matrix covalent bonds provided by the TESPT coupling agent.

Wear debris were also analyzed using XPS. These analyses have revealed that the composition of the wear debris is similar to that of the worn surface, with the presence of oxidized sulfur indicating the scission of (or at least a fraction of) the crosslinks and silica-matrix bonds. This was observed for wear debris generated with very different sizes and shapes in sulfur-vulcanized elastomer materials.

The test design ensures well-controlled isothermal conditions, meaning that the temperature rises experienced by the sample would be solely attributable to friction. Infrared measurements indicate that, under the applied conditions, the local temperature increases at the sample surface during the wear test remains very small, in the range of 1–3 °C. This suggests that the chemical modifications observed are not thermally activated but are induced by mechanical mechanisms of chain scission associated to friction.

This work confirms that two distinct types of mechanisms associated to low severity, or fatigue, wear must be considered. The first one is chemical degradation, which appears to occur similarly in all three investigated samples, despite their different reinforcing systems. The second process is mechanical and leads to quite different shapes and sizes of wear debris in the three different investigated samples.

CRediT authorship contribution statement

C. Chanal: Writing – review & editing, Writing – original draft, Methodology, Investigation, Conceptualization. **J. Galipaud:** Writing – review & editing, Investigation, Formal analysis. **B. Moreaux:** Investigation. **J.-L. Loubet:** Writing – review & editing, Supervision, Conceptualization. **P. Sotta:** Writing – review & editing, Validation, Supervision, Conceptualization.

Declaration of competing interest

The authors declare that they have no known competing financial interests or personal relationships that could have appeared to influence the work reported in this paper.

Acknowledgements

The authors would like to thank Pierre Alcouffe for providing the SEM images on the sample edge. We would like to thank Pauline Grau for her help and assistance in the definition of sample formulations. We are also grateful to Bruno Bertel for giving access to the thermal analysis equipment and assisting with the measurements and processing of the results.This study is part of the cooperative research project WEEL funded by the French National Research Agency (ANR) under the project ANR-21-CE06-0048.

Appendix A. Supplementary data

Supplementary data to this article can be found online at https://doi.org/10.1016/j.wear.2025.205753.

Data availability

Data will be made available on request.

References

[1] B. Baensch-Baltruschat, B. Kocher, F. Stock, G. Reifferscheid, Tyre and road wear particles (TRWP) - a review of generation, properties, emissions, human health risk, ecotoxicity, and fate in the environment, Sci. Total Environ. 733 (2020) 137823.
[2] A. Piscitello, C. Bianco, A. Casasso, R. Sethi, Non-exhaust traffic emissions: sources, characterization, and mitigation measures, Sci. Total Environ. 766 (2021) 144440.
[3] S. Wagner, T. Hüffer, P. Klöckner, M. Wehrhahn, T. Hofmann, T. Reemtsma, Tire wear particles in the aquatic environment - a review on generation, analysis, occurrence, fate and effects, Water Res. 139 (2018) 83–100.
[4] Z. Mané, J.-L. Loubet, C. Guerret, L. Guy, O. Sanseau, L. Odoni, L. Vanel, D. Long, P. Sotta, A new rotary tribometer to study the wear of reinforced rubber materials, Wear 306 (1) (2013) 149–160.
[5] M. Huang, M. Guibert, J. Thévenet, C. Fayolle, T. Chaussée, L. Guy, L. Vanel, J.-L. Loubet, P. Sotta, A new test method to simulate low-severity wear conditions experienced by rubber tire materials, Wear 410–411 (2018) 72–82.
[6] G. Petitet, M. Barquins, Matériaux caoutchouteux: morphologies, formulations, adhérence, glissance et usure, EPFL Press, 2008.
[7] A. Schallamach, Abrasion, fatigue, and smearing of rubber, J. Appl. Polym. Sci. 12 (2) (1968) 281–293.
[8] A.H. Muhr, A.D. Roberts, Rubber abrasion and wear, Wear 158 (1) (1992) 213–228.
[9] A.N. Gent, C.T.R. Pulford, Mechanisms of rubber abrasion, J. Appl. Polym. Sci. 3 (28) (1983) 943–960.
[10] E. Southern, A.G. Thomas, Studies of rubber abrasion, Rubber Chem. Technol. 52 (5) (1979) 1008–1018.
[11] H. Liang, Y. Fukahori, A.G. Thomas, J.J.C. Busfield, Rubber abrasion at steady state, Wear 266 (1) (2009) 288–296.
[12] E. Koliolios, S. Nakano, T. Kawamura, I. Tsumori, J.J.C. Busfield, in: Constitutive Models for Rubber XII, Taylor & Francis Group, 2022, pp. 483–488.
[13] E. Koliolios, S. Nakano, T. Kawamura, J.J.C. Busfield, Elucidation of smear wear layer structure and ageing mechanisms of filled tyre tread compounds, Polymer 300 (2024) 126982.
[14] G. Wu, P. Sotta, M. Huang, L.B. Tunnicliffe, J.J.C. Busfield, Characterization of sticky debris generated during smear wear, Rubber Chem. Technol. 96 (4) (2023) 588–607.
[15] J. Fröhlich, W. Niedermeier, H.-D. Luginsland, The effect of filler–filler and filler–elastomer interaction on rubber reinforcement, Compos. Appl. Sci. Manuf. 36 (4) (2005) 449–460.
[16] J. Ramier, C. Gauthier, L. Chazeau, L. Stelandre, L. Guy, Payne effect in silica-filled styrene–butadiene rubber: influence of surface treatment, J. Polym. Sci. B Polym. Phys. 45 (3) (2007) 286–298.

[17] K.A. Grosch, The relation between the friction and visco-elastic properties of rubber, Proc. Roy. Soc. Lond. Math. Phys. Sci. 274 (1963) 21–39.
[18] A. Le Gal, L. Guy, G. Orange, Y. Bomal, M. Klüppel, Modelling of sliding friction for carbon black and silica filled elastomers on road tracks, Wear 264 (7) (2008) 606–615.
[19] M. Thomine, J.-M. Degrange, G. Vigier, L. Chazeau, J.-M. Pelletier, P.G.L. Kapsa, G. Dudragne, Study of relations between viscoelasticity and tribological behaviour of filled elastomer for lip seal application, Tribol. Int. 40 (2) (2007) 405–411.
[20] C.D. Wagner, L.E. Davis, M.V. Zeller, J.A. Taylor, R.H. Raymond, L.H. Gale, Empirical atomic sensitivity factors for quantitative analysis by electron spectroscopy for chemical analysis, Surf. Interface Anal. 3 (5) (1981) 211–225.
[21] P. Sotta, M. Guibert, J.-L. Loubet, J. Thevenet, L. Vanel, M. Huang, Device for Measuring Rubber Wear, US Patent US11067489B2, 2017.
[22] A.M. Hottin, F. Berthier, R. Feys, J.F. Becq-Giraudon, M. Recoing, P. Freytet, R. Delbos, Carte Géol. France (1/50000), Feuille Guéret (642), Editions du Service géologique national, 1993.
[23] K. Grosch, A. Schallamach, Relation between abrasion and strength of rubber, Rubber Chem. Technol. (1966) 278–305.
[24] D. Especel, S. Matteï, Total emissivity measurements without use of an absolute reference, Infrared Phys. Technol. 37 (7) (1996) 777–784.
[25] B. Berthel, Mesures thermographiques de champs de dissipation accompagnant la fatigue à grand nombre de cycles des aciers, Université Montpellier II - Sciences et Techniques du Languedoc, France, 2007. PhD thesis.
[26] J.F. Moulder, W.F. Stickle, P.E. Sobol, K.D. Bomben, Handbook of X-Ray Photoelectron Spectroscopy, Perkin-Elmer Corporation, 1992.
[27] J.T. Gruver, K.W. Rollmann, Antioxidant properties of carbon black in unsaturated elastomers. Studies with cis-polybutadiene, J. Appl. Polym. Sci. 8 (3) (1964) 1169–1183.
[28] E.M. Bevilacqua, Carbon black as an elastomer antioxidant, Polymer Letters 5 (12) (1967) 1109–1118.
[29] M.L. Huggins, Bond energies and polarities, J. Am. Chem. Soc. 75 (17) (1953) 4123–4126.
[30] Y. Uchiyama, The effect of environment on the friction and wear of rubber, Wear 110 (3) (1986) 369–378.
[31] B.N.J. Persson, Rubber friction: role of the flash temperature, J. Phys. Condens. Matter 18 (32) (2006) 7789.
[32] N.L. Jean Denape, Aspect thermique du frottement: mise en évidence expérimentale et éléments de modélisation, Mec. Ind. 1 (6) (2000) 563–579.
[33] G. Petitet, Contribution à la compréhension des mécanismes élémentaires d'usure douce des élastomères chargés réticulés, Ecole Centrale de Lyon, France, 2003. PhD thesis.
[34] J.E. Mark, Physical Properties of Polymers Handbook, American Institute of Physics, New York, 1996.
[35] P.-L. Vuillermoz, M. Laurent, Conductivité thermique des solides. Techniques de l'Ingénieur, 1993.
[36] D. Waples, J. Waples, A review and evaluation of specific heat capacities of rocks, minerals, and subsurface fluids. Part 1: minerals and nonporous rocks, Nat. Resour. Res. 13 (2) (2004) 97–122.
[37] Y. Lin, S. Liu, J. Peng, L. Liu, The filler–rubber interface and reinforcement in styrene butadiene rubber composites with graphene/silica hybrids: a quantitative correlation with the constrained region, Compos. Appl. Sci. Manuf. 86 (2016) 19–30.